Crystal structure of bacterial cytochrome bc_1 in complex with azoxystrobin reveals a conformational switch of the Rieske iron–sulfur protein subunit

Received for publication, March 11, 2019, and in revised form, June 6, 2019 Published, Papers in Press, June 10, 2019, DOI 10.1074/jbc.RA119.008381

Lothar Esser[‡], **Fei Zhou**[‡], **Chang-An Yu**[§], **and Di Xia**[‡1]

From the [‡]*Laboratory of Cell Biology, Center for Cancer Research, NCI, National Institutes of Health, Bethesda, Maryland 20892 and the* [§]*Department of Biochemistry and Molecular Biology, Oklahoma State University, Stillwater, Oklahoma 74078*

Edited by Norma M. Allewell

Cytochrome bc_1 complexes (cyt bc_1), also known as complex III in mitochondria, are components of the cellular respiratory chain and of the photosynthetic apparatus of non-oxygenic photosynthetic bacteria. They catalyze electron transfer (ET) from ubiquinol to cytochrome *c* and concomitantly translocate protons across the membrane, contributing to the cross-membrane potential essential for a myriad of cellular activities. This ET-coupled proton translocation reaction requires a gating mechanism that ensures bifurcated electron flow. Here, we report the observation of the Rieske iron–sulfur protein (ISP) in a mobile state, as revealed by the crystal structure of cyt bc_1 from the photosynthetic bacterium *Rhodobacter sphaeroides* in complex with the fungicide azoxystrobin. Unlike cyt bc_1 inhibitors stigmatellin and famoxadone that immobilize the ISP, azoxystrobin causes the ISP-ED to separate from the cyt *b* subunit and to remain in a mobile state. Analysis of anomalous scattering signals from the iron–sulfur cluster of the ISP suggests the existence of a trajectory for electron delivery. This work supports and solidifies the hypothesis that the bimodal conformation switch of the ISP provides a gating mechanism for bifurcated ET, which is essential to the Q-cycle mechanism of cyt bc_1 function.

The cytochrome bc_1 complex (cyt bc_1 or bc_1),[2] also known as mitochondrial complex III, forms the mid-section of the cellular respiratory chain (1). It is also an essential component of the photosynthetic apparatus of purple bacteria (2). A major function of cyt bc_1 is the pumping of protons across the membrane, which is coupled to electron transfer (ET) from its substrate, ubiquinol, to cyt *c* (cyt c_2 in bacteria). Depending on the organism, protein compositions of cyt bc_1 vary from 11 subunits in humans (*Homo sapiens*, $Hsbc_1$) (3) and cows (*Bos taurus*, $Btbc_1$) (4) to three or four subunits in photosynthetic bacteria such as *Rhodobacter capsulatus* (*R. capsulatus*, $Rcbc_1$) (5) or *Rhodobacter sphaeroides* (*R. sphaeroides*, $Rsbc_1$) (6). Common to all cyt bc_1 complexes are three catalytic subunits that contain prosthetic groups: cyt *b*, containing hemes b_L and b_H; cyt c_1, containing a *c*-type heme; and the Rieske iron–sulfur protein (ISP), containing an Fe_2S_2 cluster.

The mechanism by which the cyt bc_1 carries out its ET-coupled proton translocation is known as the Q-cycle mechanism (Fig. 1) (7). This mechanism requires a quinol oxidation site (Q_o or Q_P site) near the electrochemically-positive side of the membrane and a quinone reduction site (Q_i or Q_N site) near the negative side of the membrane. The presence of the two sites has been verified by crystal structures in the presence of various Q_P and Q_N site inhibitors and by mutational studies (8–11). Essential to the Q-cycle mechanism is the bifurcated ET at the Q_P site, in which the two electrons liberated from a ubiquinol substrate follow two different paths: one electron enters the high-potential chain (ISP, cyt c_1, and cyt *c*) and the other follows the low-potential chain (b_L, b_H, and ubiquinone/ubisemiquinone). Despite the peculiarity of this proposed bifurcated ET, the Q-cycle mechanism is able to explain various experimental observations, including the H^+/e ratio, and the oxidant-induced cyt *b* reduction (12, 13). Numerous hypotheses have been proposed to provide chemical explanations for the bifurcated ET (14).

The crystal structures of mitochondrial cyt bc_1 reveal several important features. 1) In the native enzyme, the extrinsic domain of the ISP (ISP–ED), a single electron carrier mediating ET from the membrane-embedded cyt *b* to cyt c_1 in the aqueous phase, exhibits a high degree of mobility and appears in distinctly different positions in different crystal forms (4, 10, 15–17). 2) In a large number of structures, ISP–ED is clustered

This work was supported by the Intramural Research Program of the National Institutes of Health, NCI, Center for Cancer Research. The authors declare that they have no conflicts of interest with the contents of this article. The content is solely the responsibility of the authors and does not necessarily represent the official views of the National Institutes of Health.

This article contains Figs. S1 and S2 and Table 1.

The atomic coordinates and structure factors (codes 6NHH, 6NIN, and 6NHG) have been deposited in the Protein Data Bank (http://wwpdb.org/).

[1] To whom correspondence should be addressed. E-mail: xiad@mail.nih.gov.

[2] The abbreviations used are: bc_1, cytochrome bc_1; cyt, cytochrome; azo (azoxystrobin), methyl (*E*)-2-[2-[6-(2-cyano-phenoxy) pyrimidin-4-yl] oxyphenyl]-3-methoxyprop-2-enolate; b_H, high-potential heme *b*; b_L, low-potential heme *b*; $Btbc_1$, *Bos taurus* mitochondrial cyt bc_1; ET, electron transfer; famoxadone, 5-methyl-5-(4-phenoxy-phenyl)-3-phenylamino-2,4-oxazolidinedione; UHDBT, 6-hydroxy-5-undecyl-4,7-benzothiazoledione; MOAS, methyl (2Z)-3-methoxy-2-(2-[(E)-2-phenylvinyl] phenyl)acrylate; Pf, Q_P site inhibitors that fix ISP–ED conformation; Pm, Q_P site inhibitors that mobilize ISP–ED conformation; stg (stigmatellin), 2-[(3*S*,4*S*,5*S*,6*S*,7*E*,9*E*,11*E*)-4,6-dimethoxy-3,5,11-trimethyltrideca-7,9,11-trienyl]-8-hydroxy-5,7-dimethoxy-3-methylchromen-4-one; SMC, sucrose monocaprate; ISP, iron–sulfur protein; ISP–ED, extrinsic domain of ISP; $Ggbc_1$, *Gallus gallus* mitochondrial cyt bc_1; Q_P or Q_o, ubiquinol oxidation; Q_N or Q_i, ubiquinone reduction; rms, root-mean square; $Rsbc_1$, cyt bc_1 from photosynthetic bacterium *Rhodobacter sphaeroides*; PDB, Protein Data Bank; ANL, Argonne National Laboratory; APS, Advanced Photon Source; DDM, dodecyl-D-maltopyranoside; β-OG, β-octyl glucoside; Ar–Ar, aromatic–aromatic.

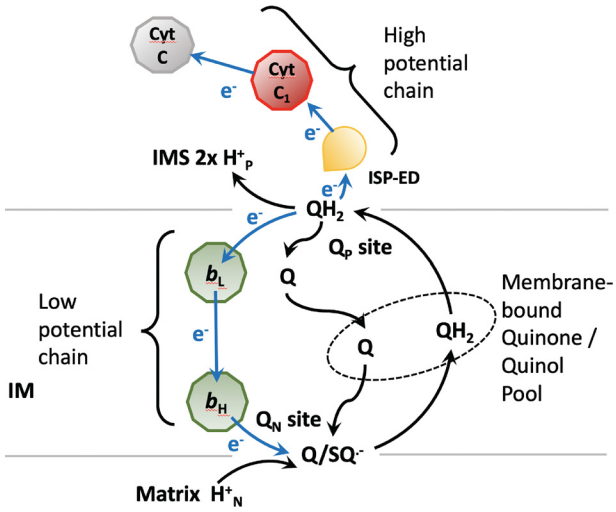

Figure 1. Q-cycle mechanism The cyt bc_1 complex can be seen as made of a high-potential chain (ISP, cyt c_1, and cyt *c*) located in the intermembrane space (*IMS*) of mitochondria and a low-potential chain (hemes b_L and b_H) embedded in the inner membrane (*IM*). There are two reaction sites: quinone reduction (Q_N) and quinol oxidation (Q_P) sites. At the Q_P site, the two electrons from a ubiquinol (QH_2) diverge: the first one taking the high-potential chain and the second one going into the low-potential chain, reducing ubiquinone/ubisemiquinone ($Q/SQ^{\cdot-}$) at the Q_N site. The Q and QH_2 at the Q_N and Q_P sites are in free exchange with those present in the membrane-bound quinone/quinol pool shown inside the *ellipse* in the *dashed line*.

at the *b*-site: an ISP-binding site on the surface of the cyt *b* subunit near the Q_P site. The distance between the Fe_2S_2 of the ISP and the cyt c_1 heme is ~31 Å, which is too great for efficient ET to the high-potential chain (18). 3) In a small number of structures, the ISP–ED is found close to cyt c_1 (c_1-site) and somewhere between the c_1-site and the *b*-site (intermediate positions) (16, 17). 4) The conformation of the ISP–ED can be modulated by two classes of cyt bc_1 inhibitors targeting the Q_P site: one class is the P_f-type, which fixes the ISP–ED at the *b*-site, and the other class is the P_m-type, which mobilizes the ISP–ED (10, 15, 19). It was thus hypothesized that the ISP–ED functions as a controlled, swiveling single electron carrier that bridges the distance from ubiquinol to cyt c_1 in the aqueous phase, accomplishing the bifurcated ET at the Q_P site (15, 20).

The ISP–ED is roughly cone-shaped and at its tapered end (the tip) is an Fe_2S_2 cluster coordinated by two internal cysteines and two surface-accessible histidine residues. This structural feature enables the ISP–ED, once oxidized, to dip into the volcanic crater-shaped binding site on the cyt *b* subunit (*b*-site), gaining access to the Q_P site. Although the ISP–ED is bound at the *b*-site, it extracts one electron as well as one proton from ubiquinol, producing transiently a ubisemiquinol free radical at the Q_P site and a reduced ISP–ED. To force a bifurcated ET to occur, the reduced ISP–ED is postulated to stay bound at the Q_P site until the remaining electron associated with the ubisemiquinol enters the low-potential chain. Subsequently, with the removal of the reaction product ubiquinone into the membrane phase, the reduced ISP–ED is released and delivers the electron to cyt c_1, while the proton enters the aqueous phase (15).

The requirement of a mobile ISP–ED for the function of cyt bc_1 was elegantly demonstrated in bacterial cyt bc_1 systems by introducing mutations that altered the mechanical flexibility of residues in the "neck" region of ISP (21, 22) and by engineering a disulfide bridge between cyt *b* and ISP–ED (23). Foreshortening the neck region or substituting flexible residues with rigid ones (Ala → Pro and Gly → Val) in the ISP inactivated the entire complex without affecting the assembly or complex integration into the membrane (24). Likewise, using a mutant cyt bc_1 that carries a K70C mutation in the ISP subunit and an A185C mutation in the cyt *b* subunit ($ISP^{K70C}Cyt b^{A185C} Rsbc_1$), Xiao *et al.* (23) showed that in an oxidizing environment that forms and maintains the disulfide bridge the enzyme's function was abolished but could be restored by reduction.

It was demonstrated that the ISP–ED of bacterial cyt bc_1 can be immobilized at the *b*-site by P_f-type inhibitors such as stigmatellin or famoxadone (6, 25). Despite the fact that a large number of mechanistic studies of the cyt bc_1 complex were conducted using photosynthetic bacteria such as *R. sphaeroides* and *R. capsulatus* for their ease of molecular manipulability and the demonstration that their enzyme's function requires the ISP–ED to be conformationally flexible, this very transition from a fixed to a mobile conformation has never been structurally demonstrated for any bacterial cyt bc_1 complex. Furthermore, the sequence of events for the ISP–ED to transition from a fixed state in the *b*-site to a mobile state and subsequently to approach the c_1-site has not been clearly defined. Although the functional significance for the existence of the *b*-site is well-established, that for the c_1-site has been controversial. The question is whether a fixed c_1-site is truly a requirement for the function of cyt bc_1. In this work, we demonstrate the existence of an ISP–ED conformation switch in bacterial cyt bc_1 by solving the crystal structure of cyt bc_1 in complex with azoxystrobin ($Rsbc_1$/azo). We further show that the ISP–ED adopts multiple positions when it is in the mobile state. This was accomplished by enhancing the anomalous signal of iron atoms by collecting data from a crystal of bovine mitochondrial cyt bc_1 in complex with azoxystrobin ($Btbc_1$/azo) at an incident wavelength of 1.739 Å near the Fe absorption edge. Our data corroborate with the highly transient nature of the c_1-state when ISP–ED is mobile (26).

Results

Structure of $Rsbc_1$, arrested in the b-state reveals the correct position of the engineered disulfide bond

We previously introduced a double-cysteine mutation in $Rsbc_1$ to show that the flexibility of the ISP–ED is important for the cyt bc_1 function (23). The mutation sites were K70C in the ISP subunit and A185C in the cyt *b* subunit, resulting in a mutant designated $ISP^{K70C}cyt b^{A185C} Rsbc_1$. To verify the correct formation of the disulfide bond, we crystallized $ISP^{K70C}cyt b^{A185C} Rsbc_1$ in the presence of stigmatellin, a known P_f-type inhibitor that arrests the ISP–ED at the *b*-site. The structure (Fig. 2*A*) of $ISP^{K70C}cyt b^{A185C} Rsbc_1$/stg was determined with three independent dimers per crystallographic asymmetric unit (Table 1). In the structure, the ISP–ED is trapped in the *b*-site, and the disulfide bridge between residues Cys-70 of the ISP and Cys-185 of cyt *b* is correctly formed (Fig. 2*B*). All three dimeric cyt bc_1 molecules, with a total of six disulfide bridges, are superimposable. Importantly, the structure

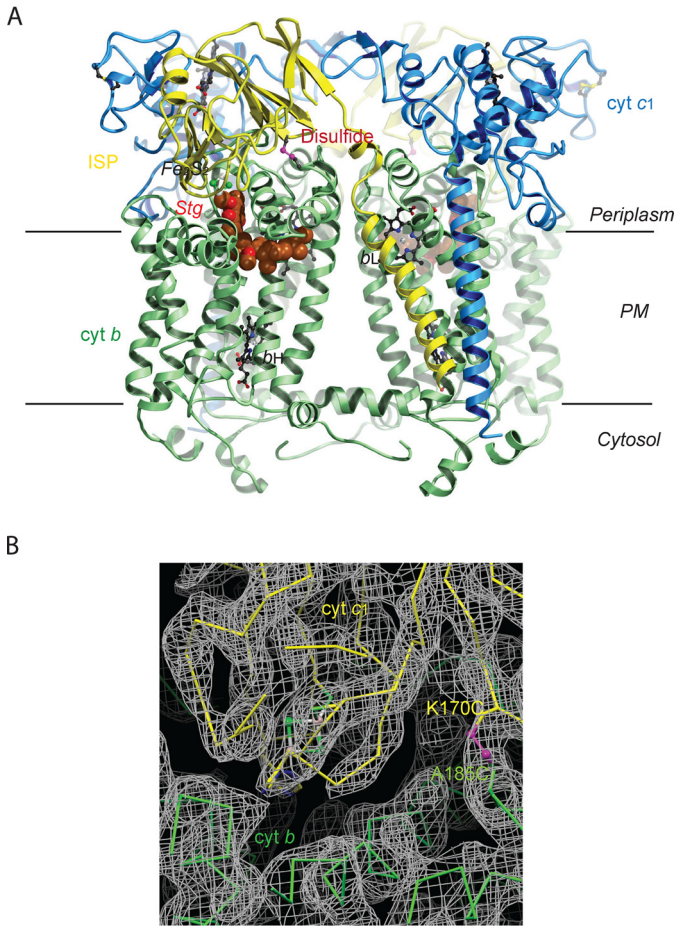

Figure 2. Structure of *Rsbc*$_1$/stg with the ISP–ED in the *b*-site. *A,* overall structure of the dimeric *Rsbc*$_1$ with the ISP–ED trapped in the *b*-site. The cyt *b* subunits are shown in *green*, cyt c_1 in *blue*, and the ISP in *yellow*. Stigmatellin is rendered as a CPK model with carbon atoms colored *brown*. The engineered disulfide bridge (ISP) Cys-70–Cys-185 (cyt *b*) is shown in *magenta*. Heme groups are depicted as *ball-and-stick* models with carbon atoms in *black*, nitrogen in *blue*, and oxygen in *red*. The Fe_2S_2 cluster of ISP is shown as *balls* with iron atoms in *orange* and sulfur in *green*. *B,* electron density in the vicinity of the disulfide bridge (*magenta*) between ISP (shown in *yellow*) and cyt *b* (shown in *green*). The continuous density around this bridge (K170C of ISP and A185C of cyt *b*) shows that it formed correctly to arrest ISP–ED in the *b*-state.

proves that the residues chosen for mutation to cysteine are properly aligned when the ISP–ED is at the *b*-site and the disulfide bridges are formed under normal oxidizing conditions. The engineered inter-subunit disulfide bond changes the position of the ISP–ED domain only slightly from its position in the WT *Rsbc*$_1$/stg complex published earlier (Fig. S1) (6).

ISP–ED is in the mobile state as revealed by the structure of Rsbc$_1$ inhibited by azoxystrobin

To demonstrate the ISP–ED conformation switch in bacterial cyt bc_1, we used a P_m-type inhibitor, namely azoxystrobin, in a crystallization experiment with *Rsbc*$_1$ (*Rsbc*$_1$/azo), as binding of azoxystrobin in *Btbc*$_1$ promotes the mobile state of the ISP–ED. This experiment was expected to be challenging, due to the enhanced mobility of the ISP–ED and with it the loss of a rigid hydrophilic surface that could contribute to crystal contacts. With just cyt c_1 remaining in a rigid conformation, the chances of crystallizing *Rsbc*$_1$/azo were considered small. Nevertheless, crystallization conditions were established after extensive screening, and the resulting crystals of *Rsbc*$_1$/azo diffracted X-rays to 3 Å resolution (Table 1). Consistent with the structures reported previously (6), crystal contacts are formed between neighboring ef1 helices through pairs of π-stacked tryptophan residues (Trp-313) flanked by molecules that appear to be lipids.

The structure of *Rsbc*$_1$/azo has at its core a cyt *b* homodimer with a total of 16 membrane-spanning helices (Fig. 3*A*) that are flanked by pairs of C-terminal helices of cyt c_1 and N-terminal helices of the ISP. The large functional head domains of both cyt c_1 and the ISP extend into the periplasm. Unlike the static head domain of *cyt* c_1, the ISP–ED is mobile and disordered in both halves of the cyt bc_1 dimer, with no clearly defined electron density to model the polypeptide chain (Fig. 3*B*). In fact, both ISP–EDs are so disordered that the Fe_2S_2 cluster can only be located with the help of its anomalous signal, which is obtained from the anomalous difference Fourier map using the coefficients F(*h,k,l*) – F(*-h,-k,-l*) with a phase of ϕ_{model} −90°. This calculation produced several peaks >3σ near the subunits cyt *b* and cyt c_1 in addition to the expected peaks for the b_L, b_H, and c_1 heme iron atoms (Table 2). However, in each case their occupancies are low compared with those of the heme groups b_L, b_H, and c_1. The highest nonheme iron peak is 6σ above average and is 19.2 Å from the c_1 heme iron. We assigned this peak to the Fe_2S_2 cluster of the ISP–ED of the second monomer (model B). A model for this ISP–ED was constructed but had a low occupancy of 0.25. It should be noted that this ISP–ED conformation is only one of many conformations that exist (see below). Indeed, structure refinement of *Rsbc*$_1$/azo with the ISP–ED included produced no better refinement statistics than without it. Furthermore, the highest Fe_2S_2 anomalous peak of model B is slightly offset (~2 Å) from that of model A (Table 2). Taken together, the binding of azoxystrobin allows the ISP–ED to be in a mobile state with no specific positional preference. This degree of mobility is also observed in mitochondrial cyt bc_1 in the structures *Btbc*$_1$/azo (PDB code 1SQB) and *Ggbc*$_1$/azo (PDB code 3L71). The latter is a homodimer with one ISP–ED (chain E) disordered and the other (chain R) ordered. It occupies the c_1' position, far from cyt *b*. It should be mentioned that the disorder of the ISP–ED is not an indication of the absence of the ISP subunit as a whole, because the N-terminal helix of the ISP is clearly visible in the electron density from residues 13 to 52 of the neck region (Fig. 3*B*).

Binding of azoxystrobin to the Q_P site of Rsbc$_1$

In each of the cyt *b* subunits, a single azoxystrobin molecule (Fig. 4*A*) is firmly bound at the Q_P site, displacing ubiquinol and thus preventing any direct reduction of the Fe_2S_2 cluster of the ISP. The toxophore of azoxystrobin is a planar *E*-β-methoxy methyl acrylate group forming a hydrogen bond (2.79 Å) through the ester's carbonyl group with the backbone amide of Glu-295 (Fig. 4*B*), which is part of the highly conserved PEWY motif. At the same time, the side chain of Glu-295 is rotated toward the aqueous phase, compared with its inward conformation when P_f-type inhibitors such as UHDBT or stigmatellin are bound (19). The flat toxophore (3-methoxy methylacrylate) is positioned between Phe-144 and Tyr-147. The attached

Table 1
Statistics on the quality of diffraction data sets of bc_1 crystals and structural models

	Rsbc$_1$/azo[a]	ISP^{K70C}cyt*b*^{A185C} *Rsbc*$_1$/stg[a]	*Btbc*$_1$/azo[a]
Diffraction data			
Space group	$P2_1$	$C2$	$I4_122$
Cell parameter (Å,°) (angles not listed equal 90°)	a = 89.31, b = 154.7, c = 100.9, β = 95.36	a = 356.7, b = 145.8, c = 162.2, β = 104.97	$a = b$ = 154.2, c = 598.1
Resolution (Å) (outer shell)	39.29–3.00 (3.02–3.00)[b]	28.79–3.60 (3.728–3.60)	27.84–2.80 (2.90–2.80)
Wavelength (Å)	1.00	0.827	1.739
R_{merge}	0.195 (0.91)	0.114 (0.73)	0.144 (1.65)
Completeness (%)	99.54 (96.14)	97.05 (95.48)	94.60 (95.74)
$\langle I/\sigma I \rangle$	8.1 (1.9)	6.72 (1.2)	32.36 (2.16)
No. of unique observations	54,666 (5,228)	90,139 (8,819)	88,694 (8,314)
Refinement			
Resolution (Å)	39.29–3.00	28.79–3.60	27.84–2.80
R_{free}	0.288 (0.382)	0.293 (0.378)	0.284 (0.397)
R_{work}	0.266 (0.377)	0.250 (0.348)	0.252 (0.362)
No. of atoms	13,927	40,362	16,342
No. of residues	1,738	5,213	2,085
No. of ligand atoms	423	1,146	537
No. of solvent molecules	0	0	119
rms deviations			
Bond length (Å)	0.005	0.003	0.006
Bond angles (°)	0.71	0.61	0.67
Ramachandran plot			
Favored, allowed (%)	94.9, 4.9	97.6, 2.4	96.0, 3.4
Outliers (%)	0.2	0.0	0.6
PDB entry	6NHH	6NIN	6NHG

[a] azo is azoxystrobin; stg is stigmatellin.
[b] Statistics for the highest-resolution shell are shown in parentheses.

o-phenyloxy ring is nearly orthogonal to the acrylate moiety due to steric constraints (Fig. 4*B*), but it is also ideally positioned to wedge between Pro-294 of the PEWY motif and Gly-158 of the cd1 helix. The pyrimidine ring forms an aromatic–aromatic (Ar–Ar) pair with Phe-298 and prevents Ile-162 of the cd1 helix from returning to a fully relaxed position. The *o*-cyano-phenoxy group is surrounded by the hydrophobic residue Met-140 and the aromatic groups of Phe-337 and Phe-301 at ideal distances for Ar–Ar interactions.

Multiple positions of the ISP–ED are also observed in the structure of mitochondrial cyt bc_1 in complex with azoxystrobin

The fact that iron atoms can appear as significant peaks in anomalous difference Fourier maps and thus mark the positions of the Fe_2S_2 clusters in *Rsbc*$_1$/azo inspired us to re-visit the structure of mitochondrial cyt bc_1 with the P_m-type inhibitor azoxystrobin bound. To study this, we grew crystals of *Btbc*$_1$ in the presence of azoxystrobin (*Btbc*$_1$/azo) and collected a diffraction data set using an incident wavelength of λ = 1.739 Å near the iron K absorption edge (FeK: 1.743 Å) (Table 1). Using a *Btbc*$_1$ crystal is particularly advantageous over other alternatives because of its stability, very high space group symmetry of $I4_122$ (highly redundant data), and non involvement of the ISP-ED in crystal contacts. The crystal structure not only shows enhanced anomalous signals for the element iron (Table 2), but indeed it dramatically improves the signal for all sulfur atoms in cofactors, standard cysteine and methionine residues, as well as those of phosphorus atoms in lipids (Fig. 5*A*). Although our re-investigation of the structure of *Btbc*$_1$/azo does not substantially differ from our previously published structure (PDB code 1SQB) or its avian counterpart (PDB code 3L71) (both were collected at 1.0 Å incident radiation), it does, however, allow better visualization of the ISP–ED in its mobile state (Table 2). Although the ISP–EDs are disordered, the presence of four >3.5σ peaks for the Fe_2S_2 clusters indicate that, despite the absence of obvious restraints (domain–domain interactions, crystal contacts), the ISP–ED still finds local minima between cyt *b* and cyt c_1 (Fig. 5*A*).

Discussion

ISP–ED conformation switch is characterized by the change from a fixed to a mobile state and induced by different types of Q_P site inhibitors

The ISP–ED conformation switch was first suggested in a structural study of mitochondrial cyt bc_1, in which different inhibitors gave rise to dramatically different peak heights in anomalous difference Fourier maps for the Fe_2S_2 cluster at its cyt *b*–binding site (10). This phenomenon was subsequently used as a basis for classification of cyt bc_1 inhibitors that target the Q_P site (19); those that give rise to strong peaks for the Fe_2S_2 cluster are called P_f-type inhibitors, and those that lead to no or weak anomalous peaks are termed P_m-type inhibitors. However, this switch between conformations is often misinterpreted as evidence that the ISP–ED moves from the fixed *b*-site to a similarly rigid c_1-site (27–29), and thus it deserves further clarification.

The accumulation of a large number of homologous structures of cyt bc_1 from different species, including bacteria, yeast, birds, and mammals, that were crystallized in different space groups and under various conditions allowed comparisons aimed at distinguishing lattice-induced stabilization of the ISP–ED from natural, low-affinity sites. However, this comparison is often biased toward ISP–ED models built by crystallographers, who naturally select the most prominent conformation and consequently ignore all the others. To overcome this deficiency, in this work we performed structure superposition

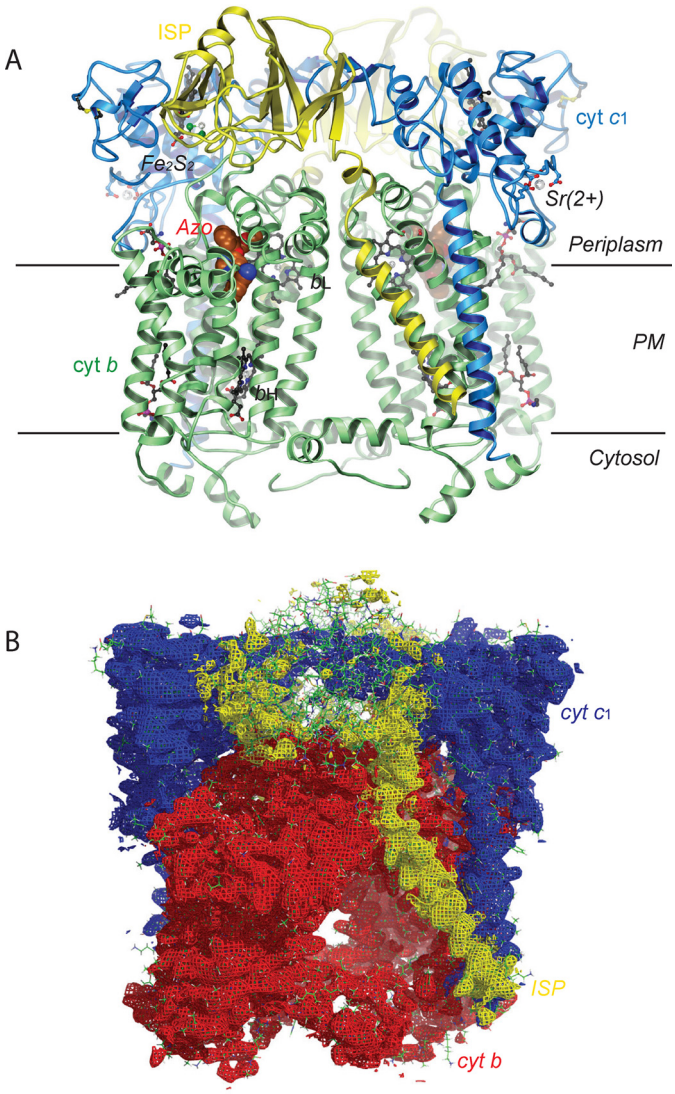

Figure 3. Structure of *Rsbc*$_1$/azo with ISP–ED disordered. *A,* two cyt *b* subunits are shown as *green ribbons* containing the b_H and b_L heme groups. Azoxystrobin is shown as a CPK model and lipid molecules as *ball-and-stick* models. The two cyt c_1 subunits with covalently linked *c*-type hemes are shown in *blue*. The bound Sr^{2+} ions (*silver spheres*) stem from a crystallization additive. Both *yellow ribbon* models of the iron–sulfur protein are highly disordered and are shown in a position that places their Fe_2S_2 clusters in or near a position with detectable anomalous signal from their iron atoms. The *parallel horizontal lines* delineate the boundary of the membrane bilayer. *B,* electron density for the *Rsbc*$_1$/azo dimer with cyt *b* in *red*, cyt c_1 in *blue*, and ISP in *yellow*. Although the N-terminal helix of ISP has a good electron density, the head domain is largely disordered.

using not only the positions of Fe_2S_2 from different models but also anomalous difference density maps, if available, resulting in a distribution of Fe_2S_2 locations in 3D space (Fig. 5*B* and Table 3). From the distribution, we observed the following. 1) When the Q_P site is occupied by the P_f-type inhibitors (stigmatelin, UHDBT, etc.), there is one strong Fe_2S_2 anomalous peak, located at the bottom of the ISP-docking site. This position is frequently referred to as the *b*-site. 2) When the Q_P site is not occupied by substrates or inhibitors, Fe_2S_2 can appear in three different positions, and its corresponding anomalous peaks are weak. The most frequent position is near the *b*-site and is displaced on average from it by 1.5 Å (*Nat site*, Fig. 5*B*). A second position, represented by one model (PDB code 1BE3), has the Fe_2S_2 near the heme c_1, a position referred to as the c_1-site. The same position was found to overlap with weak anomalous peaks from P_m-type inhibitor-bound cyt bc_1 crystals. A third position, also represented by only one model (PDB code 1BGY), is 7 Å from the second site and is referred to as the intermediate site (*Int site*, Fig. 5*B*). Again, this site also overlaps with anomalous peaks from apo- and P_m-type inhibitor-bound cyt bc_1 crystals. 3) When the Q_P site is bound with P_m-type inhibitors (azoxystrobin, MOAS, etc.), the Fe_2S_2 positions are further displaced from the apo-site, spanning the distance between the "Int" site and the "Nat" site, as exemplified by the 3.8 Å shift from the apo-site for the azoxystrobin-bound structure (Fig. 5*B*). We term this site the *b*′-site. It has a rms deviation from its mean position of 7.3 Å. There are three additional sites marked also by weak anomalous peaks. One overlaps with the c_1-site. Another was previously observed in a number of avian cyt bc_1 structures inhibited by P_m-type inhibitors (PDB code 6NHH, 3L70, etc.), referred to as the c_1′-site. The third Fe_2S_2 position has not previously been reported and is designated the *b*″-site.

Based on the distribution of the anomalous peaks and following published conventions, we propose the following. 1) ISP–ED is at the *b*-site (therefore, the cyt bc_1 is in the *b*-state) when it associates tightly with the cyt *b* subunit, permitting the first electron and proton transfer from the substrate to the ISP. The *b*-site is approximated by the binding of P_f-type inhibitors. At this position, the ISP–ED features a very large anomalous peak, and the rms deviation for the Fe_2S_2 position is 0.72 Å. 2) In the absence of substrate at the Q_P site, the ISP–ED switches to a mobile conformation, which is facilitated by the binding of P_m-type inhibitors at the Q_P site. The Fe_2S_2 cluster can appear in either the *b*′-site, *b*″-site, c_1-site, or c_1′-site, indicating that the positions of the ISP–ED are not well-determined. Thus, we further define the conformation switch of the ISP–ED as the change from a fixed state at the *b*-site to a mobile state, detached from the *b*-site (Fig. 5*B*) (15). In the fixed state, the ISP–ED docks firmly at the *b*-site with its Fe_2S_2 cluster penetrating into and being part of the Q_P site, where the substrate ubiquinol and inhibitors bind. By contrast, the ISP–ED is in the mobile state that requires the ISP–ED to be detached by at least 1.5 Å from the *b*-site, which is triggered by the displacement of the cd1/cd2 helices. It becomes apparent that the liberated ISP–ED is very mobile but may still favor distinct positions on its path to the cyt c_1 for the electron transfer. Interestingly, the c_1′-, *b*′-, and the *b*″-sites are located along the path of an arc that may define the preferred trajectory for the movement of the ISP–ED (Fig. 5*B*).

ISP–ED conformation switch is critical to the Q-cycle mechanism

The key question surrounding the bifurcated ET at the Q_P site is how the second electron of ubiquinol is prevented from following the first electron, which enters the high-potential chain consisting of ISP ($E_{m,7}$ = +285 mV for *Rsbc*$_1$), cyt c_1 ($E_{m,7}$ = +295 mV), and soluble cyt c_2 ($E_{m,7}$ = +295 mV). The

Table 2
Peak positions from anomalous difference Fourier correspond to iron positions in crystal structures of *Btbc*$_1$ and *Rsbc*$_1$

Iron center	Peak[a] height (σ)[a]	Coordinate			Modeled	Distance to c_1 heme iron
		x	y	z		
			Å			Å
***Btbc*$_1$/azo[b] data collected at 1.739 Å wavelength**						
b_L	39.0	68.81	70.76	166.09	Cyt *b*	34.6
b_H	43.5	66.93	63.74	146.91	Cyt *b*	51.4
c_1	28.0	55.93	61.79	196.89	Cyt c_1	0.0
Fe_2S_2-1	12.5	72.94	44.11	178.61	Yes as ISP	30.6
Fe_2S_2-2	7.8	68.96	45.51	189.72	No	22.1
Fe_2S_2-3	4.7	76.64	37.05	178.97	No	36.9
Fe_2S_2-4	3.5	64.79	50.95	193.99	No	14.3
***Rsbc*$_1$/azo[a] data collected at 1.0 Å wavelength**						
Monomer A						
b_L^A	8.1	1.38	3.77	32.76	Cyt b^A	34.1
b_H^A	4.6	19.78	0.88	41.62	Cyt b^A	50.6
c_1^A	6.2	−30.18	−6.78	40.06	Cyt c_1^A	0.0
$Fe_2S_2^A$-1	3.2	−17.37	16.70	−9.37	Yes as ISP	23.5
$Fe_2S_2^A$-2	3.2	−25.66	22.11	−2.47	No	13.9
$Fe_2S_2^A$-3	3.2	−12.23	9.70	−1.23	No	27.4
$Fe_2S_2^A$-4	3.2	−26.17	4.28	1.27	No	29.3
Monomer B						
b_L^B	5.5	3.64	19.04	18.87	Cyt b^B	34.1
b_H^B	5.7	23.58	19.40	13.60	Cyt b^B	50.6
c_1^B	6.4	−24.51	33.15	5.84	Cyt c_1^B	0.0
$Fe_2S_2^B$-1	6.0	−26.04	6.95	52.77	Yes as ISP	19.2
$Fe_2S_2^B$-2	3.5	−28.59	12.44	51.40	No	22.4
$Fe_2S_2^B$-3	3.6	−22.63	4.01	55.99	No	25.1

[a] The crystal of *Btbc*$_1$/azo has a space group symmetry of $I4_122$ with one monomer per crystallographic asymmetric unit. The crystal of *Rsbc*$_1$/azo has a space group symmetry of $P2_1$ with a dimer in the asymmetric unit.
[b] All anomalous difference Fourier maps were calculated using the data in the resolution range between 25 and 5 Å.

second electron actually enters the low-potential chain that is formed by two *b*-type heme groups (b_L, $E_{m,7} = -90$ mV; b_H, $E_{m,7} = +50$ mV) (30–32). The distance of ~31 Å between Fe_2S_2 and cyt c_1 heme iron, as seen in crystal structures of cyt bc_1 bound with established P_f-type inhibitors, precludes an efficient ET between the two redox groups (Fig. 6*A* and Table S1). Thus, it was proposed that the ET between Fe_2S_2 and cyt c_1 is achieved by the oscillatory motion of the iron–sulfur protein's extrinsic domain (ISP–ED). At the end point of this motion, the Fe_2S_2 and cyt c_1 are brought close enough for efficient ET (Table S1). Indeed, the ISP–ED has been modeled in crystal structures as close as 15–21 Å from the Fe-center of the *c*-type heme group (Fig. 6*A*) (17). Furthermore, the flexibility of the ISP–ED was shown to be essential for the function of cyt bc_1 in an elegant biochemical study (22). However, such a model is at odds with the kinetic measurements because the ET rate between ISP and cyt c_1 was experimentally measured at 60,000 s^{-1} for *Rsbc*$_1$ (Sadoski *et al.* (26)), whereas the enzymatic turnover rate of *Rsbc*$_1$ is only 83 s^{-1} (2.5 μmol of cyt *c*/min/nmol of cyt *b*) (33). In other words, it is not a lack of flexibility of the ISP–ED that prevents the second electron from entering the high-potential chain. Furthermore, it is unable to explain the observation that cyt *b* reduction precedes that of cyt c_1 in pre-steady–state quinol oxidation experiments (34, 35).

The ISP–ED conformation switch offers a satisfactory mechanism for bifurcated ET at the Q_P site (Esser *et al.* (15)) (Fig. 6*B*), utilizing the architecture of the enzyme that has the ability to control the docking and undocking of the ISP–ED from the cyt *b* subunit. Thus, although the single-electron carrier ISP–ED remains immobilized at the *b*-site, the electron it carries cannot be delivered to the cyt c_1 and neither can it accept a second electron; therefore, the high-potential chain is disconnected. The initial one-electron oxidation creates an unstable ubisemiquinone radical with a very-low redox potential ($E_{m,7} = -60$ mV) (36), leaving the low-potential chain (b_L, b_H, and Q/Q$^\bullet$) as the only choice for the second electron.

We previously showed that the conformation switch of the ISP–ED is achieved by modulating its affinity to cyt *b* through substrate-induced movements of the cd1/cd2 helices. Fixation of the ISP–ED at the *b*-site is due to the increased affinity of the ISP–ED to the *b*-site in the presence of P_f-type inhibitors as a result of cd1 helix movement, which alters the ISP–ED-binding site. By contrast, the P_m-type inhibitors move the cd1 helix in the opposite direction, reducing the affinity for the ISP–ED (15).

Implications concerning development of novel inhibitors that target cyt bc_1

Azoxystrobin is an effective cyt bc_1 inhibitor of both *Btbc*$_1$ and *Rsbc*$_1$. As a classical Q_P-site inhibitor of the P_m-type, the measured IC_{50} values for azoxystrobin in *Rsbc*$_1$ and *Btbc*$_1$ are 1.34 and 1.03 nM, respectively (Fig. S2), which is corroborated by the nearly identical binding mode of the inhibitor revealed by comparison of the structures of *Btbc*$_1$ and *Rsbc*$_1$ in complex with azoxystrobin (Fig. 3*B*). High-resolution structures of the complexes afford us a detailed analysis for the observed resistance against azoxystrobin in certain mutant strains of the yeast. One frequently observed mutation (G143A) in cyt *b* impedes binding and thus renders pathogens resistant to azoxystrobin (Fig. 3*C*), which is caused by the smaller gap between the highly conserved residues Pro-294 and Gly-158 (the residues Pro-271 and Gly-143 in yeast), into which the aromatic ring of azoxystrobin intercalates. Although the G143A mutation is often the sole reason for azoxystrobin resistance in

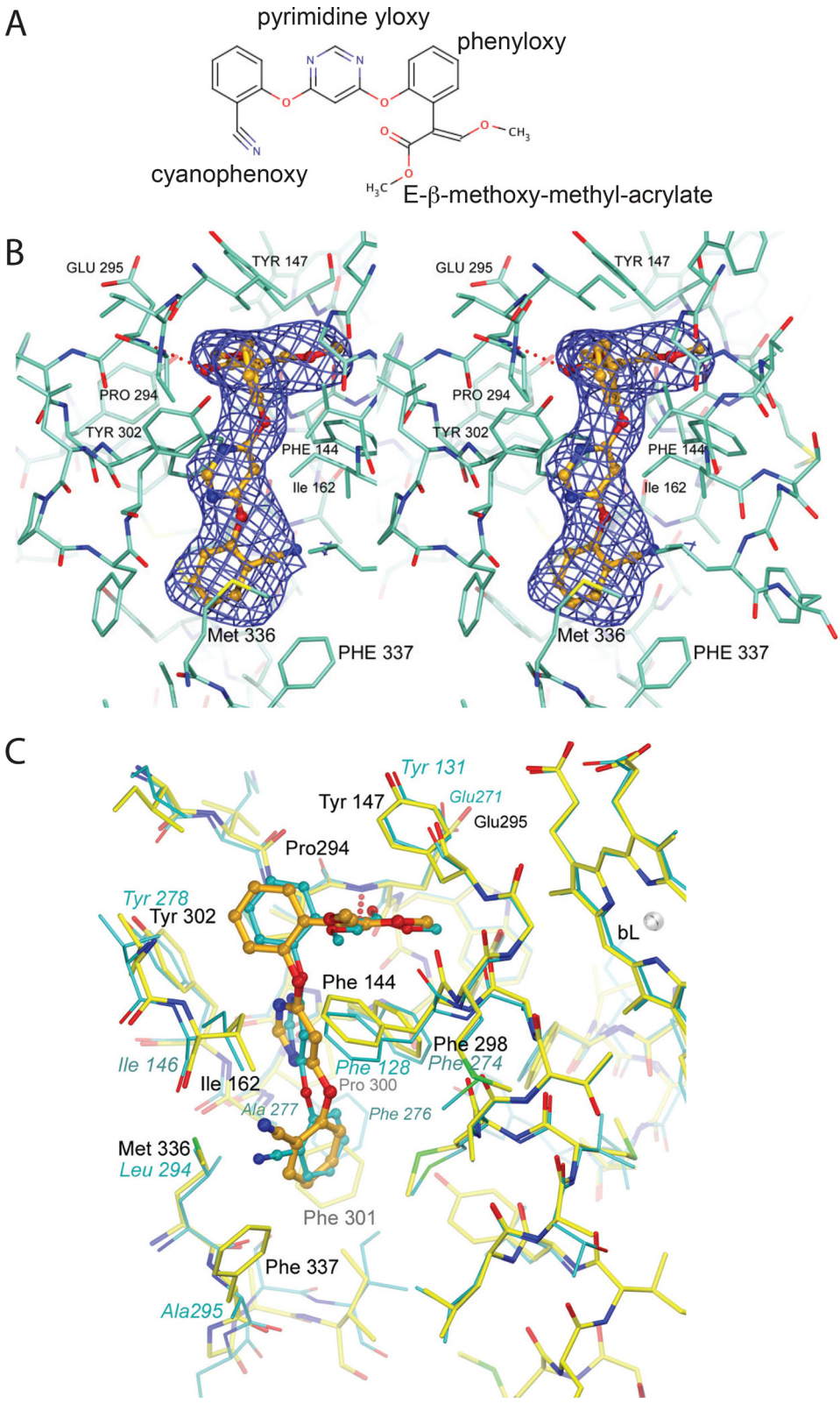

Figure 4. Chemical structure of azoxystrobin and its binding environment in *Rsbc*$_1$. *A,* chemical structure of azoxystrobin. *B,* stereographic diagram of the bound azoxystrobin in *stick* model in the Q_P pocket overlaid with the *blue* difference electron density cage for azoxystrobin. The electron density was generated with phenix.polder and contoured at 5σ. Residues lining the Q_P pocket are shown as a *stick* model. The hydrogen bond between azoxystrobin and the main-chain amide N atom of Glu-295 is shown as the *dotted line* in *red*. *C,* superposition of the Q_P site between the *Btbc*$_1$/azo and *Rsbc*$_1$/azo structures. The poses of azoxystrobin molecules bound to the Q_P sites of *Rsbc*$_1$ (*yellow sticks*) or *Btbc*$_1$ (*cyan sticks*) are nearly identical.

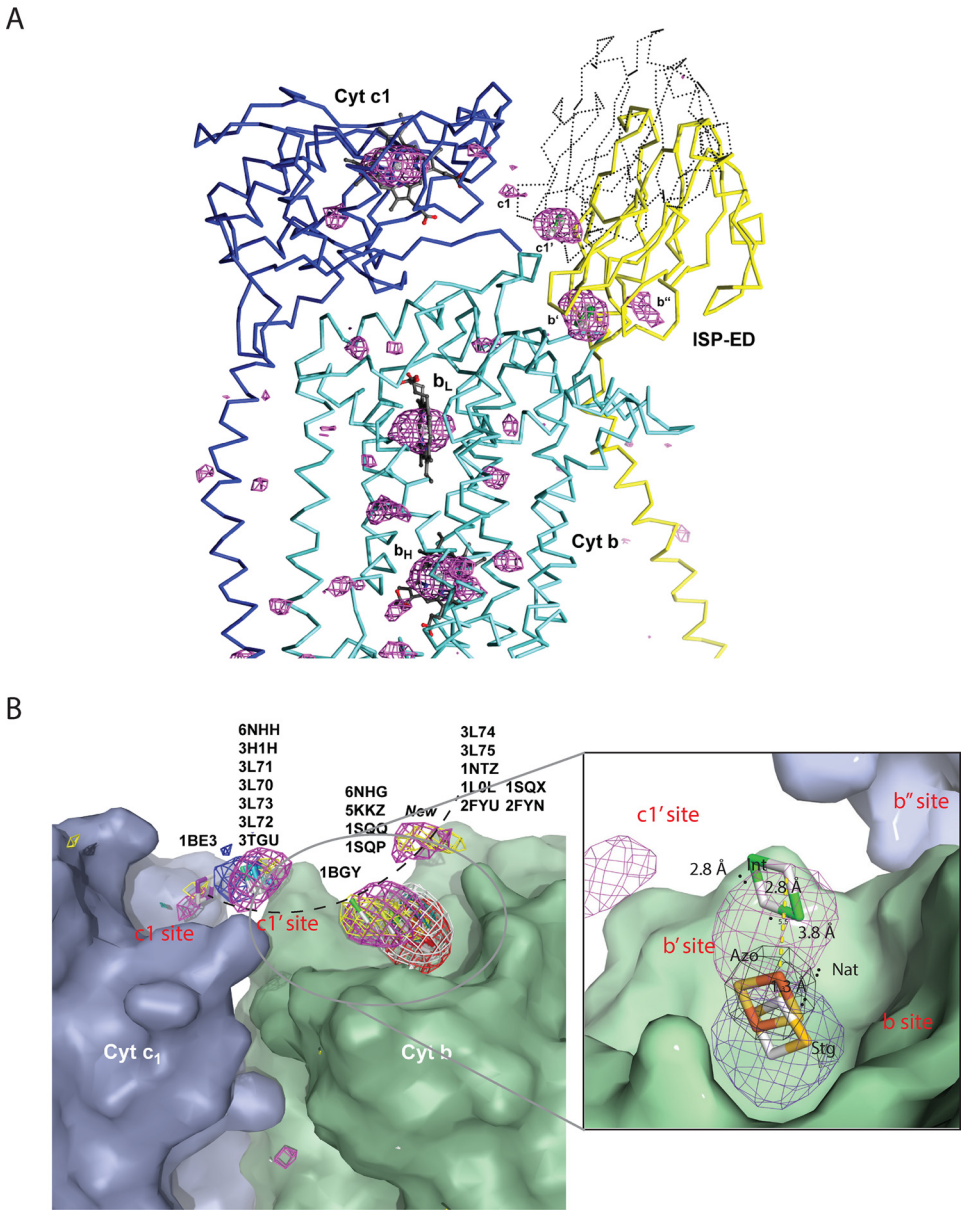

Figure 5. ISP–ED mobility of *Btbc*$_1$/azo revealed by anomalous difference Fourier. *A,* peaks from anomalous difference Fourier using X-ray diffraction data collected near the iron-absorption edge. The enhanced anomalous peaks in *Btbc*$_1$/azo (*magenta*) contoured at 3.5σ reveal four prominent sites for Fe_2S_2-labeled *b*′-, *b*″-, c_1′-, and c_1-sites, respectively. The stronger signal of the *b*′-site led to a model of ISP–ED with high-atomic displacement factors. The outline of the ISP–ED at the c_1′-position, which was not modeled in the crystal structure, is indicated by *dotted lines*. Similarly, the weaker sites *b*″ and c_1′ were not modeled. *B,* alignment of cyt bc_1 structures based on superpositions of the cyt *b* subunits to a single monomer (PDB code 6NHG and *Btbc*$_1$/azo, this work). The cyt *b* and cyt c_1 subunits superimpose well and are rendered here as the *green* and *blue* molecular surfaces, respectively. The positions of the ISP subunit are represented by positions of the Fe_2S_2 cluster (from available experimental coordinates in PDB in stick models) and by anomalous difference Fourier peaks, contoured at 3.5–3.8σ values in *red* (PDB code 1SQX, *Btbc*$_1$/stg), *white* (PDB code 2FYU, *Btbc*$_1$/jg144), *dark cyan* (PDB code 1NTZ, *Btbc*$_1$/native), *yellow* (PDB code 1SQQ, *Btbc*$_1$/MOAS), *magenta* (6NHG, *Btbc*$_1$/azo), and *blue* (PDB code 6NHH, *Rsbc*$_1$/azo). PDB identifiers correspond to the published position of the ISP–ED. The *arc in black* represents a possible trajectory for ISP movement. The *inset* features a magnified view of the ISP-docking site showing the *b*-site represented by the Fe_2S_2 position from the structure of cyt bc_1 bound with stigmatellin, the *b*′-site from structures of cyt bc_1 in the apo or P_m-type inhibitor-bound state.

fungal pathogens (with cross-resistance to numerous other strobilurin-derived pesticides), a performance penalty for the cyt bc_1 activity is incurred, as the binding of ubiquinol is also negatively affected.

The binding pose of azoxystrobin in *Rsbc*$_1$ compares well with those found in the structures of mitochondrial cyt bc_1 (*Btbc*$_1$, PDB code 1SQB) (Fig. 4*C*) and (*Ggbc*$_1$, PDB code 3L71). In the first crystal structure (PDB code 1SQB) with bound azoxystrobin, the methyl acrylate ester was assigned the s-*cis* conformation because of ambiguity in the electron density. Although the hydrogen bond to the Glu-295 amide exists even in the s-*cis* conformation, the energetically more favorable s-*trans* conformation was found in the higher-resolution structure of *Ggbc*$_1$ (PDB code 3L71) and was confirmed in our current *Btbc*$_1$/azo structure. In *Rsbc*$_1$, the bound azoxystrobin molecule adopts an overall conformation that displays a very small rms deviation from that in mitochondrial *Btbc*$_1$ after careful superposition of the cyt *b* subunits. How-

Table 3
Survey of additional peak positions in anomalous difference Fourier maps

PDB	Species	Inhibitor P/N[a]	Wavelength	Anomalous map residue range	Anomalous peak height (S/N)[b]				ISP[c] state	Additional ISP anomalous peak height (position)	Comments
					b_L	b_H	cyt c_1	ISP			
			Å	Å							
1L0N	*B. taurus*	−/−	1.0	30–5.0	15.5	18.2	10.8	5.8	b′		Native, no new Fe_2S_2 anomalous peak
1NTM	*B. taurus*	−/−	1.0	30–5.0	15.3	17.5	10.9	9.1	b′		Native, no new Fe_2S_2 anomalous peak
1SQB	*B. taurus*	Azo Pm/−	0.9189	30–5.0	10.7	13.6	8.5	5.3	b′		No new Fe_2S_2 anomalous peak
6NHG[d]	*B. taurus*	Azo Pm/−	1.736	30- 3.5	47.7	58.4	30.9	10.0	b′	4.5 (76.04, 37.51, 179.84) 6.5 (68.58, 46.21, 190.19) 3.7 (65.40, 50.47, 193.93)	Three additional anomalous peaks for Fe_2S_2, very strong anomalous signal for S and P atoms
6NHH[d]	*R. sphaeroides*	Azo Pm/−	1.0	30–5.0	8.1	4.6	6.1	5.9	c1′		No new peaks above 3.5σ cutoff. There are several peaks above 3σ (Table 1)
					5.5	5.6	6.6	3.3	c1′		
3H1K	*Gallus gallus*	IKR Pm/UQ	1.283	30–4.5	9.1	8.7	7.9	4.5	c1′		Fairly weak anomalous signal, except for Zn^{2+} and iodine of the inhibitor
					6.5	6.2	6.1	1.0	c1′		
1SQP	*B. taurus*	Myx Pm/−	1.0	30–5.0	11.5	10.9	7.9	5.3	b′		No new Fe_2S_2 anomalous peak
1SQQ	*B. taurus*	MOAS Pm /UQ	1.736	30–4.5	24.4	28.2	18.8	6.1	b′	4.20 (77.47, 36.66, 178.10) 3.70 (70.21, 45.29, 189.92)	Two new Fe_2S_2 anomalous peaks
1NU1	*B. taurus*	−/NQNO	1.2	30–4.3	11.9	15.9	7.6	13.0	b′		No significant new Fe_2S_2 anomalous peak
4D6T	*B. taurus*	−/GW 844520	0.979	30–5.0	5.8	4.0	5.4	2.7	b′		No extra anomalous Fe_2S_2 peak, very noisy, weak
					5.0	3.1	4.6	0			
4D6U	*B. taurus*	−/GSK 932121	0.979	30–5.0	2.9	3.1	3.3	3.5	b′		No extra anomalous Fe_2S_2 peak, very noisy, weak
					3.2	3.8	2.9	1.0	b′		
1SQV	*B. taurus*	UHDBT Pf/-	1.2	30–4.5	13.8	16.6	9.8	17.8	b		Very clean, no extra anomalous peak
1L0L	*B. taurus*	Fam Pf/−	1.0	30–5.0	20.7	24.2	16.9	29.4	b		Very clean, no extra anomalous peak
2FYU	*B. taurus*	JG144 Pf/−	1.009	30–5.0	15.7	17.6	13.0	24.5	b		Very clean, no extra anomalous peak
5KLV	*B. taurus*	Fen Pf/−	1.0	30- 5.0	13.9	17.8	11.5	16.9	b		No additional anomalous peak, very clean
5KKZ	*R. sphaeroides*	Fam Pf/−	1.0	30–5.0	5.5	5.7	8.0	9.8	b		No additional anomalous peak, very clean
					6.9	6.9	6.9	8.0	b		
					6.3	7.4	7.1	7.7	b		
					7.5	5.8	5.5	7.6	b		
1SQX	*B. taurus*	Stig Pf/UQ	1.0	30–5.0	12.0	11.2	11.1	15.7	b		Very clean, no extra anomalous peak
2YIU	*B. taurus*	Stig Pf/−	0.9763	30- 5.0	3.6	4.7	5.4	5.9	b		No additional anomalous peak
					5.3	2.7	5.0	6.4	b		

[a] Inhibitor or substrate bound at the P- and/or N-site.
[b] Anomalous peak height is given as number of standard deviations above mean value of the map, and a 3.5 σ cutoff value is imposed.
[c] ISP states include the *b*-state and the *b*′-state.
[d] PDB code is from this work.

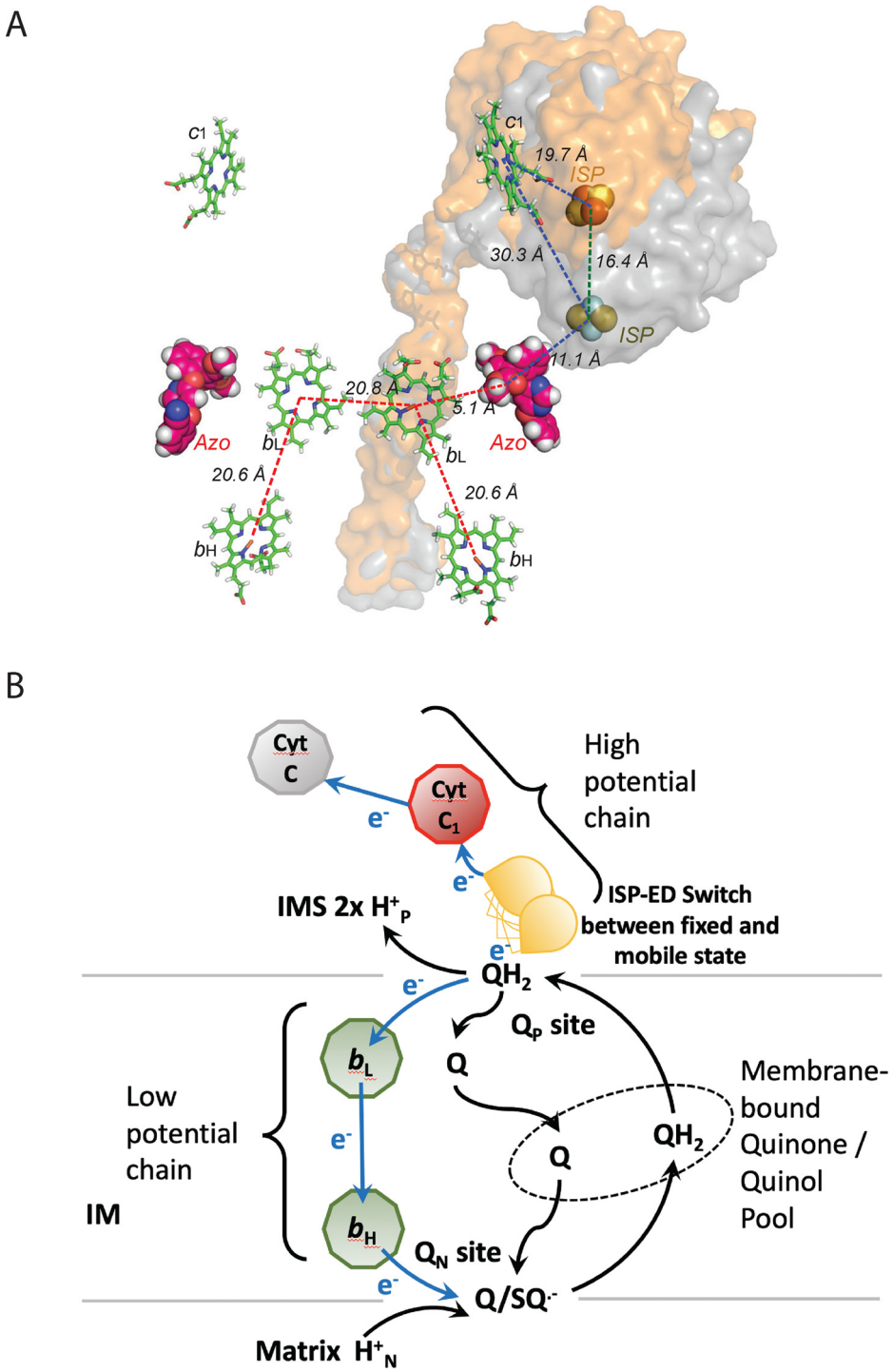

Figure 6. Controlled ISP–ED motion switch and the bifurcated ET mechanism. *A,* structure of the dimeric $Rsbc_1$/azo represented by the prosthetic groups b_L, b_H, c_1, and Fe_2S_2 in *stick* models. The bound azoxystrobin molecules are shown as *ball* models. The ISP–ED subunit was mobile and is shown as a molecular surface in the two extreme conformations: one is at the *b*-site (*gray*) and another is near the c_1′-site (*orange*). Distances between pairs of prosthetic groups are also indicated. *B,* Q-cycle mechanism is modified to incorporate the conformation switch of ISP–ED, which allows the enforcement of the bifurcated ET at the Q_P site.

ever, despite impressive overall sequence conservation of cyt *b* between species, $Rsbc_1$ features additional hydrophobic residues in the Q_P area of which azoxystrobin takes advantage. Residues Phe-301 and Phe-337 are large aromatic residues not found in mitochondrial cyt *b*, which feature instead Ala-277 and Ala-295, respectively, in $Btbc_1$ and Ala-278 and Ala-296, respectively, in $Ggbc_1$. These differences could be exploited in the future in the development of species-specific strobilurin-derived compounds.

Experimental procedures

Protein purification of $Rsbc_1$ and $Mtbc_1$

The purification procedure for $Rsbc_1$, published earlier (37), was used with minor changes to obtain protein suitable for crys-

tallization. Briefly, chromatophore membranes were prepared from cells harboring the plasmid pRKDfbcFBC$_H$, which codes for a WT *Rsbc*$_1$ lacking subunit IV ($^{\Delta\text{-IV}}$*Rsbc*$_1$), by disrupting cells with a French press followed by differential centrifugations. To purify the His$_6$-tagged *Rsbc*$_1$, the chromatophore suspensions were adjusted to a cyt *b* concentration of 25 μM with 50 mM Tris-HCl (pH 8.0 at 4 °C), containing 20% glycerol, 1 mM $MgSO_4$ and 1 mM phenylmethylsulfonyl fluoride. Dodecyl-D-maltopyranoside (DDM) solution (10% w/v) was added dropwise to a final detergent–to–protein ratio of 0.57 (mg/mg). After centrifugation, the supernatant was loaded onto a nickel-nitrilotriacetic acid column, which was washed with 6 column volumes of buffer A (50 mM Tris-HCl, pH 8.0, at 4 °C, 200 mM NaCl, 0.01% DDM), 6 column volumes of buffer A in the presence of 5 mM histidine and 4 column volumes of buffer B (50 mM Tris-HCl, pH 8.0, at 4 °C, 200 mM NaCl, 0.5% β-octyl glucoside (β-OG)) in the presence of 5 mM histidine. The desired protein fractions were eluted with buffer B containing 200 mM histidine and concentrated with Centriprep-50 to a final concentration of 300 μM.

The *Btbc*$_1$ was prepared starting from highly-purified succinate–cyt *c* reductase, as reported previously (38). The cyt *bc*$_1$ particles were solubilized by deoxycholate, and contaminants were removed by a 15-step ammonium acetate fractionation. The purified cyt *bc*$_1$ complex was recovered in the oxidized state from the precipitates formed between 18.5 and 33.5% ammonium acetate saturation. The final product was dissolved in a buffer containing 50 mM Tris-HCl, pH 7.8, and 0.66 M sucrose. The protein stock solution with a protein concentration of 30 mg/ml was stored at −80 °C. The concentrations of cyt *b* and c_1 were determined spectroscopically using millimolar extinction coefficients of 28.5 and 17.5 mM^{-1} cm^{-1} for cyt *b* and c_1, respectively.

Crystallization of Rsbc$_1$ *in complex with azoxystrobin and the double-cysteine mutant (ISP^{K70C}cytb^{A185C}Rsbc*$_1$*) inhibited by stigmatellin*

The $^{\Delta\text{-IV}}$*Rsbc*$_1$ variant at a concentration of 57 mg/ml was incubated with 3.5 mM azoxystrobin in the presence of 3.5 mM fresh sodium ascorbate for 24 h at 4 °C. The solution was diluted with a buffer containing 50 mM Tris-HCl, pH 7.5, 200 mM NaCl, 200 mM histidine, 0.5% β-octyl glucoside, 10% glycerol, 5 mM NaN_3 and 1.25 mM sodium ascorbate. This produced a 14.25 mM solution of the $^{\Delta\text{-IV}}$*Rsbc*$_1$/azo complex, which was screened for optimal crystal growth in four different concentrations of sucrose monocaprate (SMC) (0.12, 0.18, 0.24, or 0.30%) and at different concentrations of PEG 400 (5, 6, 7 or 8%). Prior to the addition of the PEG 400, each drop was augmented with 10 mM $Sr(NO_3)_2$. The best crystals grew in standard 24-well, sitting drop plates at 16 °C in the presence of 7% PEG 400 and 0.12% SMC over a reservoir of 100 mM Tris-HCl, pH 7.0, 384 mM NaCl, 16% PEG 400, 12.8% glycerol, 5 mM NaN_3, and 9 mM tris(carboxymethyl) phosphine.

The double-cysteine mutant ISP^{K70C}cyt*b*^{A185C}*Rsbc*$_1$, at a concentration of 47 mg/ml, was incubated with stigmatellin (1.4 mM final concentration) overnight at 4 °C. The resulting *Rsbc*$_1$-mutant/stigmatellin complex was diluted 3-fold (to ~16 mg/ml) with a buffer containing 50 mM Tris-HCl, pH 7.5, 200 mM NaCl, 200 mM histidine, 0.5% β-OG, and 10% glycerol. As before, 10 mM $Sr(NO_3)_2$ was added. Three different amounts of SMC (0.06, 0.12, or 0.18%) were screened for optimal crystallization with PEG 400 as the main precipitant in the range of 4–10%. Best crystal growth occurred at a temperature of 16 °C in 8% PEG 400 and 0.12% SMC.

Crystallization of Btbc$_1$ *in complex with azoxystrobin*

A solution of the purified *Btbc*$_1$ was adjusted to a final concentration of 20 mg/ml in a buffer containing 50 mM MOPS at pH 7.2, 20 mM ammonium acetate, 20% (w/v) glycerol, and 0.16% sucrose monocaprate. The inhibitor azoxystrobin (ChemService) was dissolved in DMSO to a concentration of 100 mM and mixed with native *Btbc*$_1$ in a molar ratio of 5:1. The inhibitor/*Btbc*$_1$ solution was incubated at 4 °C overnight before it was used for crystallization. This solution was set up for crystallization as described previously (Xia *et al.* (4)). Crystals of cyt *bc*1 with bound azoxystrobin appeared within 3–4 weeks and were cryo-protected at a glycerol concentration of 30–40% (w/v).

X-ray diffraction data collection, structure determination, and refinement

Rsbc$_1$ crystals were flash-frozen in liquid propane without additional cryoprotectant. A crystal of ISP^{K70C}cyt*b*^{A185C} *Rsbc*$_1$/stg diffracted X-rays to about 3.6 Å Bragg spacing at beamline 22 ID (Ser-CAT) of the Advanced Photon Source at the Argonne National Laboratory (APS, ANL) and displayed the symmetry of space group *C*2. Structure solution proceeded by rigid-body refinement of the isomorphous high-resolution trimer of *Rsbc*$_1$/stg (PDB code 2QJY). The refinement protocol was carried out initially in the absence of a disulfide bridge, resulting in maps with clear evidence for electron density between the residues forming an inter-subunit Cys–Cys bridge. The structure of the mutant was refined and rebuilt in Phenix (phenix-online.org) and COOT (Crystallographic Object Oriented Toolkit Software), respectively.

For the *Rsbc*$_1$/azo crystal, a complete data set to 3.0 Å Bragg spacing was collected. The crystal belonged to the space group $P2_1$ and contained one *Rsbc*$_1$ dimer per asymmetric unit. The structure was solved by molecular replacement (Molrep, CCP4) using a trimmed dimer from a high-resolution structure (PDB code 2QJY). While having very poor densities, the mobile head domains of ISP (residues 52 to 187) were positioned in the near-"c_1" positions based on the anomalous signal for the Fe_2S_2 cluster. The low occupancies of the mobile ISP extrinsic domains were fixed at 0.25 and grouped *b*-factor refinement was applied.

Diffraction images of a *Btbc*$_1$/azo crystal were collected at beamline 5 ID (DND-CAT, APS, ANL) specifically using an X-ray wavelength of λ = 1.739 Å at the K absorption edge of iron. The crystal diffracted initially well beyond the edge of the detector, limiting the extent of the recordable data to 2.8 Å Bragg spacing. The highly-redundant data set has strong anomalous data stemming from iron with contributions from sulfur and phosphorus atoms.

Author contributions—L. E. and D. X. conceptualization; L. E., F. Z., and D. X. data curation; L. E., F. Z., and D. X. formal analysis; L. E. and D. X. validation; L. E. and D. X. investigation; L. E. and D. X. visualization; L. E., F. Z., C.-A. Y., and D. X. methodology; L. E. writing-original draft; L. E. and D. X. writing-review and editing; C.-A. Y. and D. X. resources; D. X. supervision; D. X. funding acquisition; D. X. project administration.

Acknowledgments—We thank the staff of the beamlines SER-CAT, GM/CA, and DND at Advanced Photon Source, ANL, for assistance in X-ray diffraction data collection. We also thank George Leiman for editorial assistance. This work utilized the computational resources of the NIH HPC Biowulf Linux cluster (https://hpc.nih.gov).

References

1. Keilin, D. (1925) On cytochrome, a respiratory pigment, common to animals, yeast, and higher plants. *Proc. R. Soc. Lond. B* **98,** 312–399 CrossRef
2. Trumpower, B. L. (1990) Cytochrome bc1 complexes of microorganisms. *Microbiol. Rev.* **54,** 101–129 Medline
3. Guo, R., Zong, S., Wu, M., Gu, J., and Yang, M. (2017) Architecture of human mitochondrial respiratory megacomplex I2III2IV2. *Cell* **170,** 1247–1257.e12 CrossRef Medline
4. Xia, D., Yu, C. A., Kim, H., Xia, J. Z., Kachurin, A. M., Zhang, L., Yu, L., and Deisenhofer, J. (1997) Crystal structure of the cytochrome bc1 complex from bovine heart mitochondria. *Science* **277,** 60–66 CrossRef Medline
5. Berry, E. A., Huang, L. S., Saechao, L. K., Pon, N. G., Valkova-Valchanova, M., and Daldal, F. (2004) X-ray structure of *Rhodobacter capsulatus* cytochrome bc1: comparison with its mitochondrial and chloroplast counterparts. *Photosynth. Res.* **81,** 251–275 CrossRef Medline
6. Esser, L., Elberry, M., Zhou, F., Yu, C. A., Yu, L., and Xia, D. (2008) Inhibitor complexed structures of the cytochrome *bc*1 from the photosynthetic bacterium *Rhodobacter sphaeroides* at 2.40 Å resolution. *J. Biol. Chem.* **283,** 2846–2857 CrossRef Medline
7. Trumpower, B. L. (1990) The protonmotive Q cycle. Energy transduction by coupling of proton translocation to electron transfer by the cytochrome *bc*1 complex. *J. Biol. Chem.* **265,** 11409–11412 Medline
8. Brandt, U., Schägger, H., and von Jagow, G. (1988) Characterisation of binding of the methoxyacrylate inhibitors to mitochondrial cytochrome *c* reductase. *Eur. J. Biochem.* **173,** 499–506 CrossRef Medline
9. Gao, X., Wen, X., Esser, L., Quinn, B., Yu, L., Yu, C. A., and Xia, D. (2003) Structural basis for the quinone reduction in *bc*1 complex: a comparative analysis of crystal structures of mitochondrial cytochrome *bc*1 with bound substrate and inhibitors. *Biochemistry* **42,** 9067–9080 CrossRef Medline
10. Kim, H., Xia, D., Yu, C. A., Xia, J. Z., Kachurin, A. M., Zhang, L., Yu, L., and Deisenhofer, J. (1998) Inhibitor binding changes domain mobility in the iron–sulfur protein of the mitochondrial *bc*1 complex from bovine heart. *Proc. Natl. Acad. Sci. U.S.A.* **95,** 8026–8033 CrossRef Medline
11. Schnaufer, A., Sbicego, S., and Blum, B. (2000) Antimycin A resistance in a mutant *Leishmania tarentolae* strain is correlated to a point mutation in the mitochondrial apocytochrome *b* gene. *Curr. Genet.* **37,** 234–241 CrossRef Medline
12. Lawford, H. G., and Garland, P. B. (1973) Proton translocation coupled to quinol oxidation in ox heart mitochondria. *Biochem. J.* **136,** 711–720 CrossRef Medline
13. Wikström, M. K., and Berden, J. A. (1972) Oxidoreduction of cytochrome *b* in the presence of antimycin. *Biochim. Biophys. Acta* **283,** 403–420 CrossRef Medline
14. Xia, D., Esser, L., Tang, W. K., Zhou, F., Zhou, Y., Yu, L., and Yu, C. A. (2013) Structural analysis of cytochrome *bc*1 complexes: implications to the mechanism of function. *Biochim. Biophys. Acta* **1827,** 1278–1294 CrossRef Medline
15. Esser, L., Gong, X., Yang, S., Yu, L., Yu, C. A., and Xia, D. (2006) Surface-modulated motion switch: capture and release of iron–sulfur protein in the cytochrome bc1 complex. *Proc. Natl. Acad. Sci. U.S.A.* **103,** 13045–13050 CrossRef Medline
16. Iwata, S., Lee, J. W., Okada, K., Lee, J. K., Iwata, M., Rasmussen, B., Link, T. A., Ramaswamy, S., and Jap, B. K. (1998) Complete structure of the 11-subunit bovine mitochondrial cytochrome bc1 complex [see comments]. *Science* **281,** 64–71 CrossRef Medline
17. Zhang, Z., Huang, L., Shulmeister, V. M., Chi, Y. I., Kim, K. K., Hung, L. W., Crofts, A. R., Berry, E. A., and Kim, S. H. (1998) Electron transfer by domain movement in cytochrome bc1. *Nature* **392,** 677–684 CrossRef Medline
18. Moser, C. C., Page, C. C., Farid, R., and Dutton, P. L. (1995) Biological electron transfer. *J. Bioenerg. Biomembr.* **27,** 263–274 CrossRef Medline
19. Esser, L., Quinn, B., Li, Y. F., Zhang, M., Elberry, M., Yu, L., Yu, C. A., and Xia, D. (2004) Crystallographic studies of quinol oxidation site inhibitors: a modified classification of inhibitors for the cytochrome bc1 complex. *J. Mol. Biol.* **341,** 281–302 CrossRef Medline
20. Esser, L., Yu, L., Yu, C., and Xia, D. (2008) Insights into the mechanisms of quinol oxidation in cytochrome bc1 in light of the structure of bacterial complex. *Biophys. Rev. Lett.* **2,** 229–257 CrossRef
21. Tian, H., White, S., Yu, L., and Yu, C. A. (1999) Evidence for the head domain movement of the Rieske iron–sulfur protein in electron transfer reaction of the cytochrome *bc*1 complex. *J. Biol. Chem.* **274,** 7146–7152 CrossRef Medline
22. Tian, H., Yu, L., Mather, M. W., and Yu, C. A. (1998) Flexibility of the neck region of the Rieske iron–sulfur protein is functionally important in the cytochrome *bc*1 complex. *J. Biol. Chem.* **273,** 27953–27959 CrossRef Medline
23. Xiao, K., Yu, L., and Yu, C. A. (2000) Confirmation of the involvement of protein domain movement during the catalytic cycle of the cytochrome *bc*1 complex by the formation of the intersubunit disulfide bond between cytochrome *b* and the iron–sulfur protein. *J. Biol. Chem.* **275,** 38597–38604 CrossRef Medline
24. Darrouzet, E., Valkova-Valchanova, M., and Daldal, F. (2000) Probing the role of the Fe-S subunit hinge region during Q(o) site catalysis in *Rhodobacter capsulatus* bc(1) complex. *Biochemistry* **39,** 15475–15483 CrossRef Medline
25. Esser, L., Zhou, F., Zhou, Y., Xiao, Y., Tang, W. K., Yu, C. A., Qin, Z., and Xia, D. (2016) Hydrogen bonding to the substrate is not required for Rieske iron–sulfur protein docking to the quinol oxidation site of complex III. *J. Biol. Chem.* **291,** 25019–25031 CrossRef Medline
26. Sadoski, R. C., Engstrom, G., Tian, H., Zhang, L., Yu, C. A., Yu, L., Durham, B., and Millett, F. (2000) Use of a photoactivated ruthenium dimer complex to measure electron transfer between the Rieske iron–sulfur protein and cytochrome c(1) in the cytochrome bc(1) complex. *Biochemistry* **39,** 4231–4236 CrossRef Medline
27. Crofts, A. R. (2004) The cytochrome bc1 complex: function in the context of structure. *Annu. Rev. Physiol.* **66,** 689–733 CrossRef Medline
28. Iwata, M., Björkman, J., and Iwata, S. (1999) Conformational change of the Rieske [2Fe-2S] protein in cytochrome bc1 complex. *J. Bioenerg. Biomembr.* **31,** 169–175 CrossRef Medline
29. Izrailev, S., Crofts, A. R., Berry, E. A., and Schulten, K. (1999) Steered molecular dynamics simulation of the Rieske subunit motion in the cytochrome bc1 complex. *Biophys. J.* **77,** 1753–1768 CrossRef Medline
30. Dutton, P. L., and Jackson, J. B. (1972) Thermodynamic and kinetic characterization of electron-transfer components *in situ* in *Rhodopseudomonas sphaeroides* and *Rhodospirillum rubrum*. *Eur. J. Biochem.* **30,** 495–510 CrossRef Medline
31. Prince, R. C., and Dutton, P. L. (1977) Single and multiple turnover reactions in the ubiquinone-cytochrome b-c2 oxidoreductase of *Rhodopseudomonas sphaeroides*: the physical chemistry of the major electron donor to cytochrome c2, and its coupled reactions. *Biochim. Biophys. Acta* **462,** 731–747 CrossRef Medline
32. Prince, R. C., Lindsay, J. G., and Dutton, P. L. (1975) The Rieske iron–sulfur center in mitochondrial and photosynthetic systems: Em/pH relationships. *FEBS Lett.* **51,** 108–111 CrossRef Medline
33. Xiao, K., Liu, X., Yu, C. A., and Yu, L. (2004) The extra fragment of the iron–sulfur protein (residues 96–107) of *Rhodobacter sphaeroides* cytochrome bc1 complex is required for protein stability. *Biochemistry* **43,** 1488–1495 CrossRef Medline

34. Hansen, K. C., Schultz, B. E., Wang, G., and Chan, S. I. (2000) Reaction of *Escherichia coli* cytochrome bo3 and mitochondrial cytochrome bc1 with a photoreleasable decylubiquinol. *Biochim. Biophys. Acta* **1456,** 121–137 CrossRef Medline
35. Zhu, J., Egawa, T., Yeh, S. R., Yu, L., and Yu, C. A. (2007) Simultaneous reduction of iron–sulfur protein and cytochrome bL during ubiquinol oxidation in cytochrome bc1 complex. *Proc. Natl. Acad. Sci. U.S.A.* **104,** 4864–4869 CrossRef Medline
36. Robertson, D. E., Prince, R. C., Bowyer, J. R., Matsuura, K., Dutton, P. L., and Ohnishi, T. (1984) Thermodynamic properties of the semiquinone and its binding site in the ubiquinol-cytochrome *c* (*c*2) oxidoreductase of respiratory and photosynthetic systems. *J. Biol. Chem.* **259,** 1758–1763 Medline
37. Xiao, Y. M., Esser, L., Zhou, F., Li, C., Zhou, Y. H., Yu, C. A., Qin, Z. H., and Xia, D. (2014) Studies on inhibition of respiratory cytochrome bc1 complex by the fungicide pyrimorph suggest a novel inhibitory mechanism. *PLoS ONE* **9,** e93765 CrossRef Medline
38. Yu, L., Yang, S., Yin, Y., Cen, X., Zhou, F., Xia, D., and Yu, C. A. (2009) Analysis of electron transfer and superoxide generation in the cytochrome bc1 complex. *Methods Enzymol.* **456,** 459–473 CrossRef Medline

Crystal structure of bacterial cytochrome bc_1 in complex with azoxystrobin reveals a conformational switch of the Rieske iron–sulfur protein subunit

Lothar Esser, Fei Zhou, Chang-An Yu and Di Xia

J. Biol. Chem. 2019, 294:12007-12019.
doi: 10.1074/jbc.RA119.008381 originally published online June 10, 2019